

# A Solid Electrolyte Based on Electrochemical Active $\text{Li}_4\text{Ti}_5\text{O}_{12}$ with PVDF for Solid State Lithium Metal Battery

Qi Zhou, Xiaoyan Yang, Xaosong Xiong, Qianyu Zhang,\* Bohao Peng, Yuhui Chen, Zhaogen Wang, Lijun Fu, and Yuping Wu\*

In parallel with researches unveiling the nature and mechanism in solid state battery, numbers of investigations have been pursuing methods to stabilize their performance as well as to reduce the cost. Simple preparation and earth-abundant ingredients are preconditions for a solid state electrolyte to be suitable for scalable production. In this work, a commercial anode active material, spinel  $\text{Li}_4\text{Ti}_5\text{O}_{12}$ , is introduced for the first time, which has high ionic conductivity to sustain high rate charge/discharge with considerable high performance/cost ratio, into poly(vinylidene fluoride) to achieve a composite solid electrolyte. The membrane solid electrolyte containing 80 wt% of the  $\text{Li}_4\text{Ti}_5\text{O}_{12}$  (LTO-8) shows outstanding ionic conductivity of  $2.87 \times 10^{-4} \text{ S cm}^{-1}$  at 35 °C and inhibits electronic conductive network. The self-sacrificed interface contributes to the stabilized performance of the composite.  $\text{Li}||\text{LiFePO}_4$  cells with LTO-8 present a discharge specific capacity of 150 mAh g<sup>-1</sup> at 0.5C and a considerable average specific capacity of 119 mAh g<sup>-1</sup> under 5C in 400 cycles, demonstrating its excellent working performance. This investigation provides promising application of  $\text{Li}_4\text{Ti}_5\text{O}_{12}$  for solid state electrolytes, which is superior to the reported solid state electrolytes in comprehensive performance, and surely paves another commercial way to solid state batteries.

## 1. Introduction

In wave of sustainable economics, lithium ion batteries, which have achieved great success in the portable equipment industries because of its high energy density, are attracting more interests for their crucial roles in electric vehicles and renewable energy systems.<sup>[1]</sup> Along with the pursuit to higher energy

density and larger battery pack, difficulty of battery management accompanied with safety issues also emerges, drawing great concerns of public to solid state batteries (SSBs).<sup>[2]</sup> By replacing the ignitable organic liquid electrolytes (LE) with solid state electrolytes (SSEs), flammability of devices is supposed to be largely eliminated.<sup>[3,4]</sup> Besides, bipolar-stacked design with lithium anode realized by SSEs with a high mechanical strength could further burst the energy density of SSBs.<sup>[5]</sup>

However, prior to implementation of solid-state batteries, inadequate properties and complicated manufacture process of SSEs remain issues to overcome.<sup>[6]</sup> Other than ionic conductivity that inferior to liquid electrolytes, performances of SSEs are greatly restricted by undesirable electrode/electrolyte interfacial nature, in either chemistry or physics.<sup>[7]</sup> Numerous researchers have discussed poor stability of oxide-type SSEs against lithium metal anode.<sup>[8,9]</sup> Transition element containing

SSEs like  $\text{Li}_{3x}\text{La}_{(2/3-x)}\text{TiO}_3$  (LLTO)<sup>[10]</sup> and  $\text{Li}_{1+x}\text{Al}_x\text{Ge}_{2-x}(\text{PO}_4)_3$  (LAGP)<sup>[11]</sup> could undergo a fast and constant reduction to form an inserting interphase consisting of ionic/electronic mixed conductive species, followed with short circuit or physical deform of SSEs causing cell failure.<sup>[12]</sup> Garnet-type  $\text{Li}_7\text{La}_3\text{Zr}_2\text{O}_{12}$  (LLZO) was found electrochemically stable against lithium metal, but suffers from contact losing with anode because its rigidity and lithiophobic surface.<sup>[13]</sup> Sulfide-based SSEs like thiophosphates ( $\text{Li}_2\text{S}-\text{P}_2\text{S}_5$ ) mostly suffers from undesired performance at cathode side caused by chemical deterioration and the space charge effect.<sup>[14]</sup>

As incompetent nature of SSE materials themselves, many efforts were made to build an ideal system with heterogeneous interface. Surface treatments by vapor deposition, magnetron sputtering,<sup>[15]</sup> chemical soaking<sup>[16]</sup> or physical coating<sup>[17]</sup> were conducted to form an artificial layer on SSEs. The interphase that consist of Al,<sup>[18]</sup> Ge,<sup>[19]</sup> liquid alloy,<sup>[20,21]</sup> graphite,<sup>[22]</sup>  $\text{ZnO}$ <sup>[23]</sup> or  $\text{C}_3\text{N}_4$ <sup>[24]</sup> could change the surface to lithophilic and thus improve  $\text{Li}|\text{SSE}$  contact. The compounds including ionic liquids,<sup>[25]</sup> conductive polymers<sup>[26]</sup> and salts like  $\text{LiF}$ ,<sup>[27]</sup> exhibiting thermodynamic stability against the electrodes, were considered ideal interphase to inhibit electrochemical decomposition of SSEs. Element doping coupled with hierarchy design also achieved visible enhancements with less side effect on ion transport.<sup>[28,29]</sup>

Q. Zhou, X. Yang, X. Xiong, B. Peng, Y. Chen, Z. Wang, L. Fu, Y. Wu  
State Key Laboratory of Materials-oriented Chemical Engineering  
School of Energy Science and Engineering

Nanjing Tech University  
Nanjing, Jiangsu 211816, China  
E-mail: wuyp@fudan.edu.cn

Q. Zhang  
College of Materials Science and Engineering  
Sichuan University  
Chengdu, Sichuan 610064, China  
E-mail: zhangqianyu@scu.edu.cn

Y. Wu  
School of Energy and Environment  
South East University  
Nanjing, Jiangsu 211189, China

The ORCID identification number(s) for the author(s) of this article can be found under <https://doi.org/10.1002/aenm.202201991>.

DOI: 10.1002/aenm.202201991

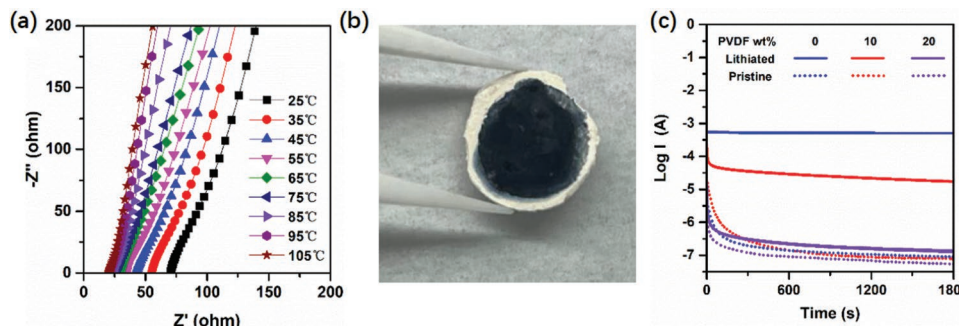


**Figure 1.** a) EIS plot of pure  $\text{Li}_4\text{Ti}_5\text{O}_{12}$  pellet under different temperature; b) the digital photo of  $\text{Li}_4\text{Ti}_5\text{O}_{12}$  after contacting with lithium metal foil; c) chronoamperometry curve of pristine/lithiated pellets with PVDF addition under 0.5 V.

Though massive strategies were explored so far, the feasibility of a SSE system is confined by not only its electrochemical property, but also the dilemma between performance and cost.<sup>[30]</sup> Expensive raw materials, strict synthesis/storage condition, including high temperature sintering and inert gas protection, have kept the high cost of SSEs and a complicate surface treatment could raise the price further.<sup>[31]</sup>

Composite solid electrolytes (CSEs) are a feasible strategy to address interfacial issues and cost dilemma as well. Although most polymer electrolytes such as poly(ethylene oxide) (PEO),<sup>[32]</sup> poly(vinylidene fluoride) (PVDF)<sup>[33]</sup> or polyacrylonitrile (PAN)<sup>[34]</sup> exhibit high ionic conductivity at room temperature by modification, this drawback is less important compared to interface contact.<sup>[35]</sup> With rational design, polymers with electronic insulation and electrochemical inertness could avoid materials like LATP,<sup>[36]</sup> LLTO,<sup>[37]</sup> LPS<sup>[38]</sup> from interfacial reaction by serving as a protective interlayer. Various structures like asymmetry, hierarchy, 3D scaffold and alignment were designed to improve interface nature, meanwhile maintain high ionic conductivity and thermal stability of CSEs.<sup>[39–41]</sup>

In this work, a rare-noticed inorganic conductive material, spinel lithium titanate  $\text{Li}_4\text{Ti}_5\text{O}_{12}$ , was for the first time investigated as an SSE through a simple compositing strategy. Widely applied as commercial anode active material, pristine  $\text{Li}_4\text{Ti}_5\text{O}_{12}$  can undergo fast charge and discharge even without carbon coating and owns low cost and good chemical stability under ambient atmosphere.<sup>[42]</sup> In comparison with solid state electrolytes material like LLZO, whose price could be over 2000 \$ kg<sup>-1</sup>,  $\text{Li}_4\text{Ti}_5\text{O}_{12}$  is much cheaper, about 50 \$ kg<sup>-1</sup>. The electrochemical activity of  $\text{Li}_4\text{Ti}_5\text{O}_{12}$  under negative potential induced a mixed conductive interphase, which largely improved electrochemical behavior at anode interface. The composite membrane with optimal  $\text{Li}_4\text{Ti}_5\text{O}_{12}$  loading not only exhibited a high ionic conductivity but also formed stable interface with electrodes. The Li|LiFePO<sub>4</sub> cell applying the composite solid state electrolyte attained an outstanding cycling stability and high rate performance. This work provides an easy and practical way to produce SSE and SSBs.

## 2. Results and Discussion

### 2.1. Nature of $\text{Li}_4\text{Ti}_5\text{O}_{12}$

The ion transport ability of  $\text{Li}_4\text{Ti}_5\text{O}_{12}$  were first test on the pellet consisted of pure powder, showing a considerable room

temperature conductivity of  $3.67 \times 10^{-4} \text{ S cm}^{-1}$  (Figure 1a). Similar to LLTO and LATP, the electrochemical active  $\text{Li}_4\text{Ti}_5\text{O}_{12}$  could be easily reduced to electronic conductive Ti(III) species.<sup>[43]</sup> Electronic conductivity could boost further electrochemical reaction, forming an inserting interphase that could penetrate the bulk electrolytes and result in cell failure.<sup>[44]</sup> The pellet made of pure  $\text{Li}_4\text{Ti}_5\text{O}_{12}$  undergoes fast reduction upon contact with lithium metal as observed from appearance, the contact area turns to deep blue (Figure 1b). The lithium metal cell applying pure  $\text{Li}_4\text{Ti}_5\text{O}_{12}$  as SSEs leads to immediate short circuit because the electronic conductive  $\text{Li}_{4+x}\text{Ti}_5\text{O}_{12}$  phase will be produced soon and expand to the whole  $\text{Li}_4\text{Ti}_5\text{O}_{12}$  pellet resulting in an electronic conductive path.

To restrain the reaction, PVDF was added into the pellet by physical mixing and the electronic conductivity of the sample was evaluated by the chronoamperometry under 0.5 V (Figure 1c). PVDF could deliver considerable film-formation ability, electronic insulation and chemical stability, and acted as a favorable choice for this research. Pure  $\text{Li}_4\text{Ti}_5\text{O}_{12}$  exhibits the steady current that ascent serval 5 orders of magnitude after contacting with lithium metal foil for 24 h, shifting from electronic isolative to semi conductive. The 10 wt% of PVDF could reduce the electronic conductivity from  $10^{-4}$  to  $10^{-6} \text{ S cm}^{-1}$  for lithiated state. The pellet with 20 wt% of PVDF has less rise on electronic conductivity and still could be regard as isolator after contact with lithium metal ( $2.8 \times 10^{-9} \text{ S cm}^{-1}$ ). PVDF was confirmed to suppress interphase insertion of  $\text{Li}_4\text{Ti}_5\text{O}_{12}$ . Of course, its influence to electrochemical property will be studied further.

### 2.2. Characterization of the CSEs

Hence, to further investigate the practicability of  $\text{Li}_4\text{Ti}_5\text{O}_{12}$  and effect of PVDF polymer, CSEs consisting of 80, 60, and 40 wt% of  $\text{Li}_4\text{Ti}_5\text{O}_{12}$  with PVDF, labeled LTO-8, LTO-6 and LTO-4, respectively, were synthesized by a simple casting method (Figure 2a). XRD pattern of samples (Figure S1, Supporting Information) shows sharp crystalline peaks that could be indexed to spinel lithium titanium oxide  $\text{Li}_4\text{Ti}_5\text{O}_{12}$  (PDF#72-0426) and two weak broad lumps nearing  $20.3^\circ$  and  $39.0^\circ$  that correspond to PVDF.

The thermal stability could be visually compared from the appearance of LTO-X during heating treatment (Figure 2b). After 10 min of heating under 120 °C, slight deformation started

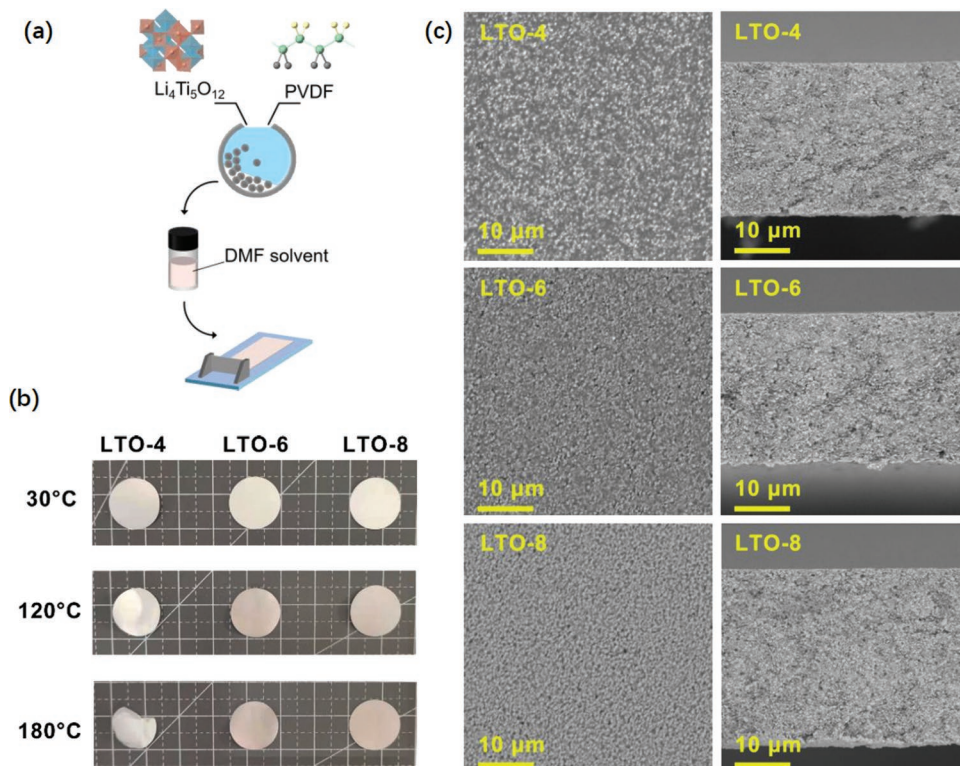


**Figure 2.** a) Preparation process of LTO-X, b) appearance evolution after heating test, and c) SEM images at surface and cross section.

to occur for LTO-4 and LTO-6. When temperature further rises to 180 °C, LTO-4 shows server shrinkage as PVDF starts to melt, while LTO-8 barely changes after heating. The enhancement of thermal tolerance could originate from high content of LTO, also acting as an inorganic filler in the composite.

SEM graphs (Figure 2c) of LTO-4 with relatively less  $\text{Li}_4\text{Ti}_5\text{O}_{12}$  loading shows a typical polymer-dominant dispersion with smooth surface where particles uniformly dispersed in PVDF matrix. Variously, surface and inner of LTO-6 still maintained a particle-in-polymer inner section with a higher  $\text{Li}_4\text{Ti}_5\text{O}_{12}$  concentration. As the particle further increased, LTO-8 becomes a ceramic-dominant composite, in which PVDF mainly served as binder to fill the gaps of compacted particles, forming a rough particle-rich surface.

Ion transport ability was first evaluated by EIS test on SS|LTO-X|SS cells (Figure S2, Supporting Information). A drop of LE (10  $\mu\text{L}$ , mass ratio 0.6:1 to the LTO film) was added to wet the electrode/CSE interface and gel PVDF to make  $\text{Li}^+$  cation transportable. The conductivity of LTO-X shows an exponentially rising trend when  $\text{Li}_4\text{Ti}_5\text{O}_{12}$  loading is increased from 40 to 80 wt%, as presented in Arrhenius plot (Figure 3a). The LTO-8 exhibits the highest conductivity, reaching  $2.87 \times 10^{-4} \text{ S cm}^{-1}$  at 35 °C, which is an order of magnitude higher than LTO-6 ( $2.18 \times 10^{-5} \text{ S cm}^{-1}$ ), while LTO-4 only shown a conductivity of  $4.56 \times 10^{-6} \text{ S cm}^{-1}$ . The monotonic trend in slope could be also observed in Arrhenius plot of LTO-4, LTO-6 and LTO-8, of which the activation energy was estimated to be 0.258, 0.189 and 0.086 eV, respectively. especially at lower temperature. In CSEs with high polymer content, the lithium migration mainly occurs in polymer phase.<sup>[45,46]</sup> Inorganic fillers have

been proposed to enhance ion transport in polymer region by improving chain mobility and ionic dissociation, which supports the enhancement in ionic conductivity from LTO-4 to LTO-6.<sup>[47,48]</sup> With further increasing of inorganic conductor, the migration in polymer could be physically block and ion transport mechanism would convert from polymer-dominated to ceramic-dominated.<sup>[33,49]</sup> Ionic conductivity of LTO-8 reaches to the same order of magnitude of pure  $\text{Li}_4\text{Ti}_5\text{O}_{12}$ , implying that a solid phase path via the inorganic conductors is more efficient for ionic conduction than polymer electrolyte.<sup>[50]</sup>

The linear sweep voltammetry (LSV) curve (Figure 3b) shows a similar electrochemical window of LTO-X. No obvious current peak is observed until potential reached 5 V, which is adequate for cooperating with  $\text{LiFePO}_4$  cathode (LFP) with a cutoff voltage of 4.2 V (vs  $\text{Li}^+/\text{Li}$ ) was carried to reveal the ion transfer behavior at lithium-electrolyte interface. The  $\text{Li}^+$  transfer numbers ( $t_{\text{Li}^+}$ ) from chronoamperometry method (Figure 3c) were estimated to be 0.53, 0.77, and 0.87 in LTO-4, LTO-6, and LTO-8, respectively. The interaction between  $\text{Li}_4\text{Ti}_5\text{O}_{12}$  and ions in the PVDF gel is supposed to enhance transfer selective by restrain anion motivation. As the content of  $\text{Li}_4\text{Ti}_5\text{O}_{12}$  increases, the transport mechanism tends to be single  $\text{Li}^+$  ion conductor, making  $\text{Li}^+$  transfer number closer to 1.

In the EIS plots of  $\text{Li}|(\text{LTO-X})|\text{Li}$  cells, the semicircles corresponding to charge transfer behavior enlarged with increasing PVDF polymer (Figure 3d). The decreased  $\text{Li}|\text{CSEs}$  interface impedance with increasing  $\text{Li}_4\text{Ti}_5\text{O}_{12}$  could indicates a more intimate interface contact or faster lithium transfer for  $\text{Li}_4\text{Ti}_5\text{O}_{12}$ -dominating surface compared to PVDF gel dominating, which is also confirmed form Tafel curve (Figure S3,

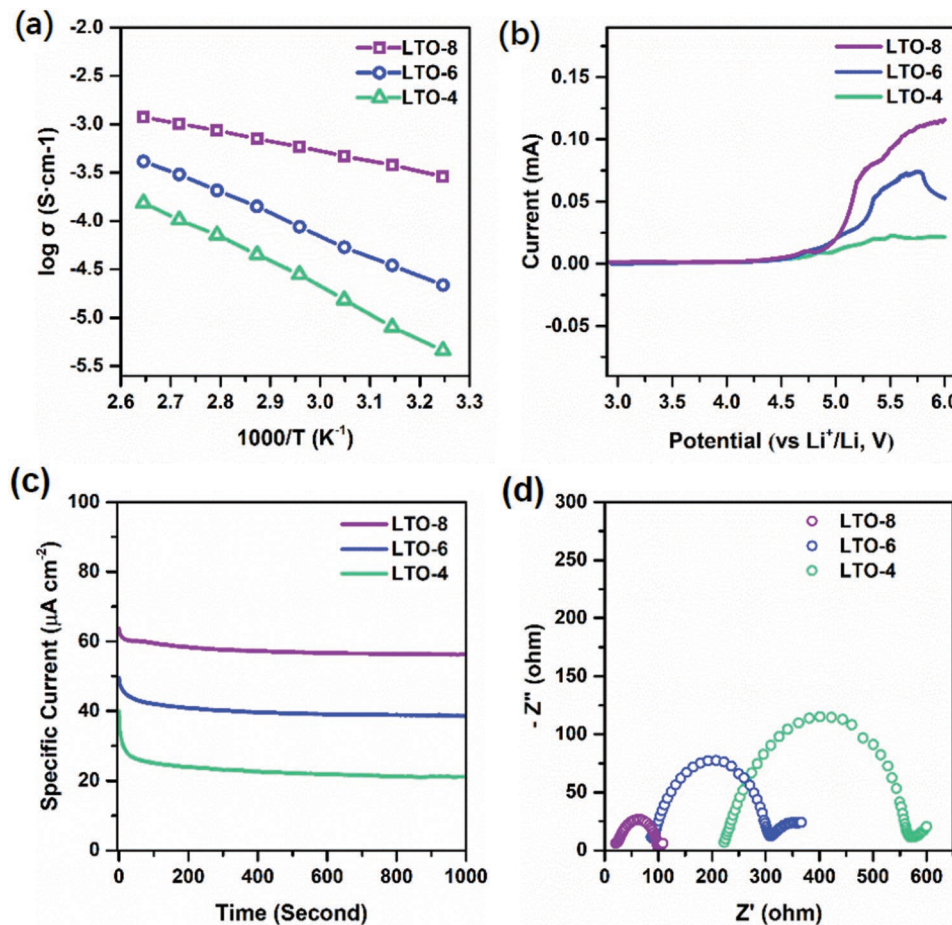


**Figure 3.** Electrochemical characteristics of LTO-X. a) Arrhenius plot, b) liner scanning curve, c) chronoamperometry curve under 10 mV, and d) EIS plots of Li|Li symmetric cells.

Supporting Information). The exchange current density ( $i_0$ ) was estimated to be 0.26, 0.23, and 0.15  $\mu\text{A cm}^{-2}$  for LTO-8/6/4, respectively, supporting the inference that charge transfer kinetics could be accelerated with high content of  $\text{Li}_4\text{Ti}_5\text{O}_{12}$ .

Over all, the significant role  $\text{Li}_4\text{Ti}_5\text{O}_{12}$  participate in ion conduction is proven, and the optimal results on ionic conductivity and transport selectivity are achieved by LTO-8. So far maximizing inorganic proportion could be the optimal strategy to boost electrochemical property, however, remaining the stability uncertified. As previously mentioned,  $\text{Li}_4\text{Ti}_5\text{O}_{12}$  is a vulnerable material, and its concentration could make CSEs easily short circuit when employing lithium metal anode. It is necessary to verify the tolerance with lithium metal and the role of  $\text{Li}_4\text{Ti}_5\text{O}_{12}$  in interface construction.

### 2.3. Li Metal Anode Interface

Symmetric Li/LTO-X/Li cells were shortly cycled with step rising current (Figure 4a). The sudden drops of voltage profile suggest the cell failure of LTO-4 and LTO-6 under the critical current 0.9 and 2.3  $\text{mA cm}^{-2}$ , respectively, while LTO-8 shows an ordered profile as specific current density reaching 4  $\text{mA cm}^{-2}$ .

In galvanostatically symmetric Li stripping/plating process (Figure 4b), LTO-X with less LTO underwent a faster failure. Voltage profile of Li|LTO-4|Li exhibits strong turbulence before its total failure (Figure S4, Supporting Information). Li|LTO-6|Li has relatively smaller polarization, but also meets a sudden voltage drop in 20 h. The fast short circuit could be attributed to lithium penetration fostered by large over potentials in LTO-4/6.<sup>[51]</sup> indicating the negligible effect of scattered  $\text{Li}_4\text{Ti}_5\text{O}_{12}$  particles on dendrite suppression. In contrast, cells with LTO-8 behaved steadily with a stable over-voltage of only 40 mV in 500 h.

The result opposite to previous intuition that the composite solid electrolytes with richest vulnerable material were supposed to be less stable, but shows the best stability and sustains the largest current with lithium anode.

To unveil the impact of  $\text{Li}_4\text{Ti}_5\text{O}_{12}$  to lithium metal anode interface, Li|LTO-X|Cu were assembly and discharged to reach certain lithium loading. Some  $\text{Li}_4\text{Ti}_5\text{O}_{12}$  particles appeared as the light points on Li surface due to their intimate contact to lithium metal and the production of electronic conduction  $\text{Li}_{4+x}\text{Ti}_5\text{O}_{12}$  phase (Figure 4c). Applying LTO-4, the surface of copper foil was covered with numerous lithium needles. It could also be observed that similar lithium needles taking roots in gap of loose lithium clump on copper foil with LTO-6. The

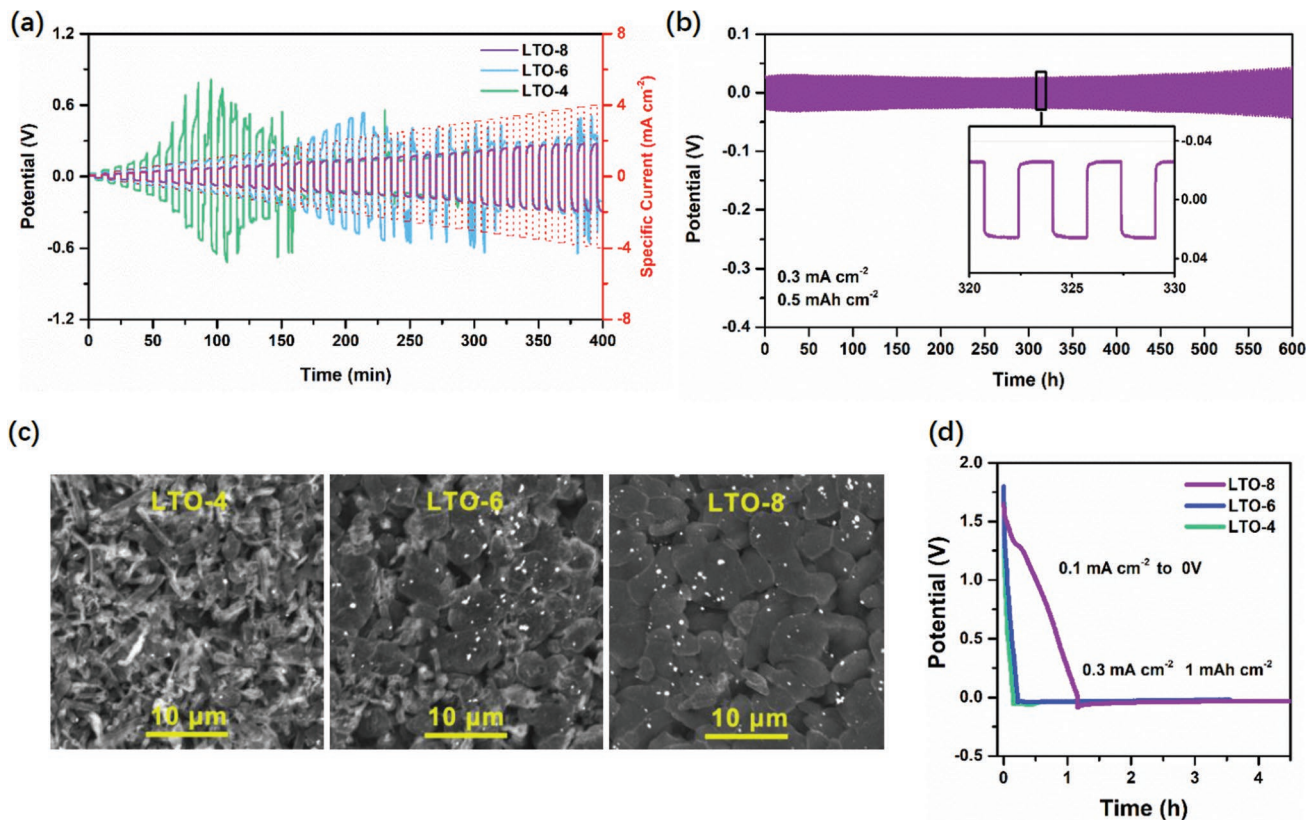


**Figure 4.** Electrochemical characterizations on Li|LTO-X interface. a) Voltage profile of symmetric cells with LTO-X cycled under step rising current density and b) profile of LTO-8 in galvanostatic cycling, c) lithium-deposited morphology, and d) voltage profiles of Cu|LTO-X|Li cells during lithium plating.

dendrites could dissociate interface contact and deteriorate field distribution, resulting in enlarged interface resistance. Poor ionic conductivity and inhomogeneous electrical field originating from uneven contact surface could promote deeper penetration of lithium whisker into the electrolyte, ending in cell short circuit. As cells with LTO-6 exhibited a mitigated condition compared to LTO-4, richer  $\text{Li}_4\text{Ti}_5\text{O}_{12}$  content could improve lithium-plating behaviour, but still failed to prevent whisker penetrating. In comparison, LTO-8 attained densely packed deposition that ellipsoid-like lithium laid intimately on copper collector with spherical nucleus rather than dendrite-like lithium observed by the edge of bulks.

The difference on initial lithium plating process offered a clue. LTO-4 and LTO-6 spent 8 min and 13 min to reach 0 V, while a 1.25 V plateau last more than 1 h is observed for LTO-8 (Figure 4d). One reasonable explanation for long activation time before lithium plating could be the electrochemical reduction of  $\text{Li}_4\text{Ti}_5\text{O}_{12}$  (from  $\text{Ti}^{4+}$  to  $\text{Ti}^{3+}$ ) driven by electric field at Cu|LTO-8 interface, as  $\text{Li}_4\text{Ti}_5\text{O}_{12}$  could also act as electrochemical active material with a plateau about 1.55 V versus  $\text{Li}^+/\text{Li}$ . For LTO-4/6,  $\text{Li}_4\text{Ti}_5\text{O}_{12}$  phase is insulated in PVDF matrix and only surface particles that directly contact with Li electrode would be lithiated, making the plateaus too short to be observed. However, highly concentrated  $\text{Li}_4\text{Ti}_5\text{O}_{12}$  could adjoin to each other in LTO-8, which make it possible to transport lithium ion as well as electron through solid-solid contact between particles.

Through electronic conductive path, the electric field could extend across the interface, resulting in a little larger activation capacity for lithium insertion.

Raman spectra could provide an evidence (Figure 5a). First,  $\text{Li}_4\text{Ti}_5\text{O}_{12}$  samples were lithiated to certain lithium loading to standardize the chemical state (SI). The spectra of pristine  $\text{Li}_4\text{Ti}_5\text{O}_{12}$  shows five characteristic peaks corresponding to five Raman-active modes ( $\text{A}_{1g} + \text{E}_g + 3\text{F}_{2g}$ ) of  $\text{Fd}3\text{m}$  space group. Three major Raman bands at 230, 421, and 670  $\text{cm}^{-1}$  could be assigned to bending vibration of Ti–O bonds ( $\text{F}_{2g}$ ), asymmetric stretching vibration of the Li–O bonds ( $\text{E}_g$ ), and symmetric vibration of Ti–O bonds ( $\text{A}_{1g}$ ), respectively.<sup>[52]</sup> With increasing lithium insertion, Li–O bond length is decreased and local structural changes of  $\text{LiO}_6$  octahedron is induced, resulting in evolution of  $\text{E}_g$  mode.<sup>[53]</sup> The  $\text{E}_g$  peak shifts toward red direction from 420  $\text{cm}^{-1}$  for  $\text{Li}_4\text{Ti}_5\text{O}_{12}$  to 380  $\text{cm}^{-1}$  for  $\text{Li}_7\text{Ti}_5\text{O}_{12}$  with decreasing intensity, which could regard as a reference for  $\text{Li}_{4+x}\text{Ti}_5\text{O}_{12}$  state. Raman spectra for LTO-8 disassembled from discharged Cu|Li cells were tested to verify  $\text{Li}_4\text{Ti}_5\text{O}_{12}$  state at the surface and the inner of the LTO-4, 6, and 8 electrolytes.  $\text{Li}_4\text{Ti}_5\text{O}_{12}$  at anode-electrolyte interface was lithiated to the state between  $\text{Li}_6\text{Ti}_5\text{O}_{12}$  to  $\text{Li}_7\text{Ti}_5\text{O}_{12}$ , while the bulk has spectra closer to pristine state. The Raman spectra indicate that lithiation in LTO-8 is still confined at interface region, which could be attributed to electric field distribution across electrolyte bulk. In consequence of semi conductivity of lithiated species and

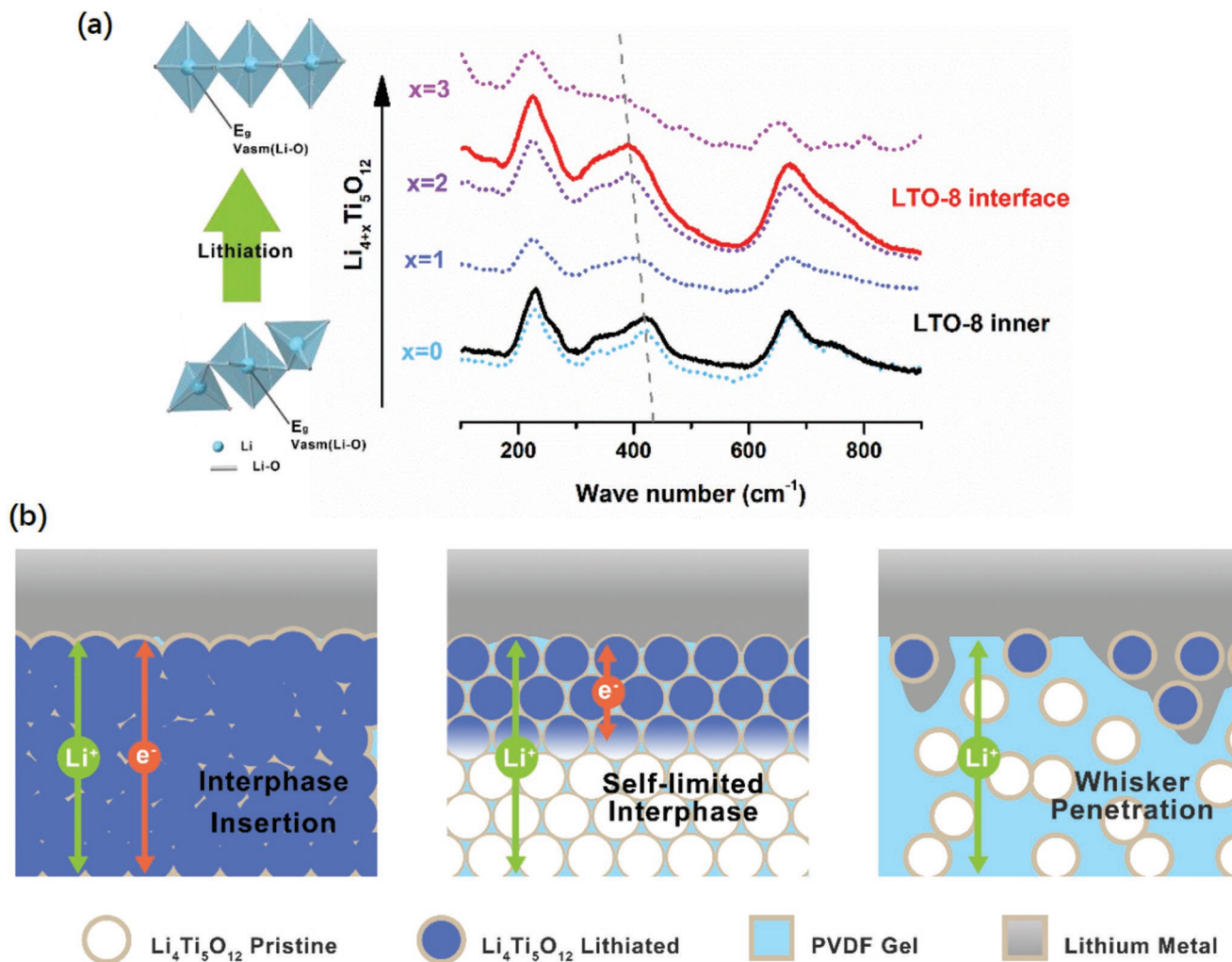


**Figure 5.** a) Raman spectra and schematic illustration of local structure evolution of Li-O in  $\text{Li}_4\text{Ti}_5\text{O}_{12}$  during lithiation; b) schematic illustration about the influence of  $\text{Li}_4\text{Ti}_5\text{O}_{12}$  density to  $\text{Li}|\text{LTO-X}$  interface.

inert PVDF phase, electric potential rises with increase depth, until it is insufficient to reach reduction potential of  $\text{Li}_4\text{Ti}_5\text{O}_{12}$ . Assuming  $\text{Li}_6\text{Ti}_5\text{O}_{12}$  is the average state of lithiated phase,  $0.1 \text{ mAh cm}^{-2}$  of activation capacity is estimated to convert 5% of overall  $\text{Li}_4\text{Ti}_5\text{O}_{12}$  to mixed ionic/electronic interphase, which accounts for about  $2 \mu\text{m}$  thickness in LTO-8.

It has been widely proposed that an artificial interlayer with mixed ionic/electronic conductivity could greatly improve interface between electrode and SSEs.<sup>[54,55]</sup> In LTO-X, lithiated  $\text{Li}_4\text{Ti}_5\text{O}_{12}$  could serve as mixed conductive phase, but only effective at particular proportion (Figure 5b). Excessive  $\text{Li}_4\text{Ti}_5\text{O}_{12}$  concentration could cause constant insertion of lithiated reaction because inadequate resistance, resulting short circuit after full penetration. In low  $\text{Li}_4\text{Ti}_5\text{O}_{12}$  content CSEs, particles are separated in polymer matrix and could not form a continue phase for ion or electron transport. Only when  $\text{Li}_4\text{Ti}_5\text{O}_{12}$  is in an appropriate range, 80 wt% in this work, the lithiated interphase could form and be limited at surface region and work as a functional interlayer in contact with lithium metal anode. Electrochemical activity

of the interphase could enlarge the charge transfer area, which explain reduced interface resistance with increasing  $\text{Li}_4\text{Ti}_5\text{O}_{12}$ . The interlayer with mixed ionic/electronic conductivity could redistribute electric flux along the interface, guarantee homogeneous electrical field that promotes uniform lithium plating,<sup>[56]</sup> thus sustaining intimate  $\text{Li}|\text{LTO-8}$  contact that reduce interface impedance and restrain dendrite growth.<sup>[57]</sup>

#### 2.4. SSBs Performances

The promotional effect of  $\text{Li}_4\text{Ti}_5\text{O}_{12}$  on cathode performance was reported to stabilize interface chemistry and reduce interface impedance.<sup>[58]</sup> Researchers also found  $\text{Li}_4\text{Ti}_5\text{O}_{12}$  interposing layer could mitigate the space charge layer between  $\text{LiCoO}_2$  and sulfide solid electrolytes by its electronic insulation and intermediate chemical potential.<sup>[59]</sup> As LTO-8 has achieved acceptable stability against Li metal anode, it is supposed to work in SSBs coupling  $\text{LiFePO}_4$  cathode.

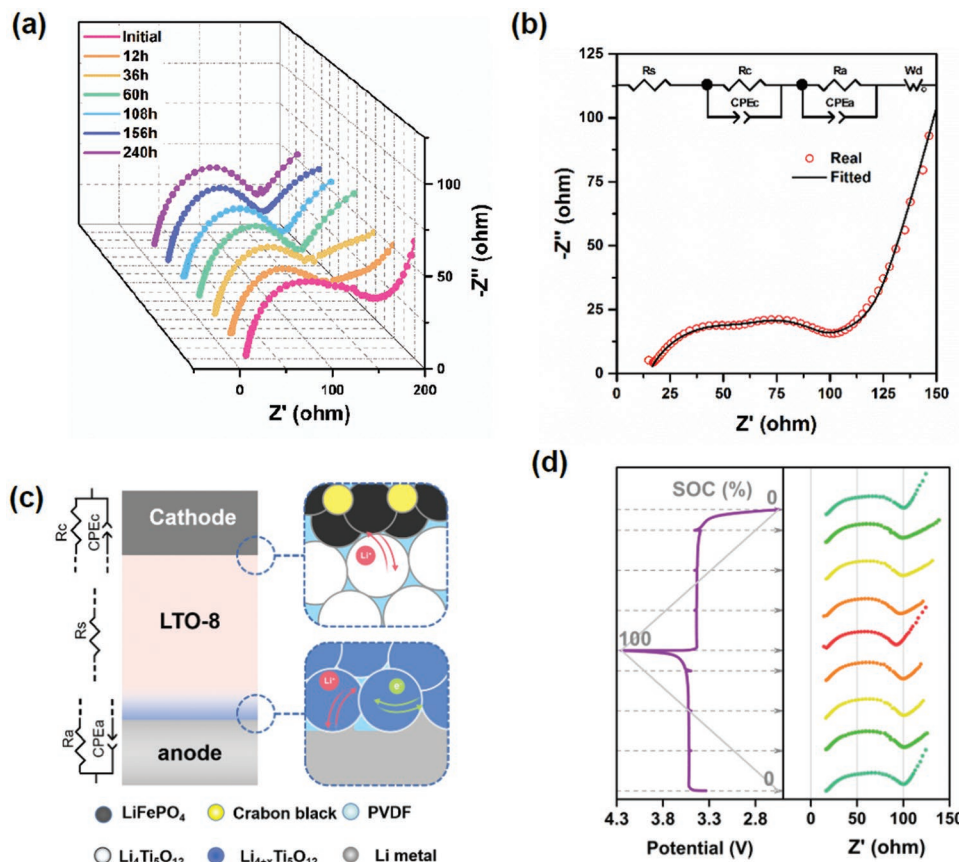


**Figure 6.** EIS characterization of Li|LTO-8|LFP cells. a) Impedance spectra during aging; b) equivalent circuit model and c) its schematic illustration; d) evolution of the cell impedance in different state of SOC.

The cyclic voltammetry curves of Li|LTO-8|LFP cell (Figure S5a, Supporting Information) show one couple of typical redox peaks of LiFePO<sub>4</sub> at 3.31 and 3.58 V, providing a considerable reaction reversibility.

The EIS plot of just assembled Li|LTO-8|LFP cells is similar to the typical model of lithium metal batteries. The curve includes a diagonal straight line at low frequency, semicircles at intermediate frequency and the intercepts at high frequency, respectively, corresponding to Warburg diffusion, interface impedance and bulk resistance (Figure 6a). During first 12 h, the semicircle shrunk from 128 to 118  $\Omega$ , because of the formation of mixed conductive interphase that improved Li|LTO-8 contact. For the following 200 h, the impedance slightly increased to 120  $\Omega$  due to erosion of the added liquid electrolyte and possible interphase reactions.<sup>[60]</sup>

The interface impedance are fitted into two elements in equivalent circuit model (Figure 6b). The semicircles at higher frequency ( $10^3$  Hz) are assumed to be cathode interface impedance and the one at lower frequency ( $10^2$  Hz) present anode side (Figure 6c). From impedance plots at different state of charge (SOC), a constant bulk resistance is sustained, indicating the lithiated interphase is still confined under negative current. (Figure 6d).<sup>[61]</sup> In the half cycle, total interface resistance declined from 73 to 68  $\Omega$ , and recovered to original value in succeeding discharge. The evolution of charge transfer impedance could be described by synergy of changes on solid

state diffusion, state of active material as well as contact area changing.<sup>[61,62]</sup> The second semicircle mainly contributed to the impedance change according to fitted results (details presented in the Supporting Information), which could ascribe to interface regenerate during lithium plating and striping at anode interface.<sup>[63]</sup> The impedance fluctuation in different SOC is quite small and reversible, stating a stable working state of LTO-8 so far.

The long-term performance of the cells is in line of our exception (Figure 7a), maintained a stable specific capacity of 150 mAh g<sup>-1</sup> over 250 cycles with a high columbic efficiency above 99.7% at 0.5C (assuming 1C = 170 mA g<sup>-1</sup>). Changes of voltage profile are ignorable after 10th cycle, performing an outstanding redox reversibility with a steady voltage hysteresis of 60 mV (Figure S5b, Supporting Information). Cells with LTO-6 and LTO-4 were assembled and tested as well, showing undesired performance and fast cell failure as the result of high resistance and interface degradation (Figure S6, Supporting Information).

The cell applying LTO-8 cycled under 0.2C, 0.5C, 1C, 2C, 3C, and up 5C deliver considerable discharge capacities of 154, 150, 145, 141, 135, and 121 mAh g<sup>-1</sup>, respectively (Figure 7b), with the potential hysteresis ramping from 60 to 480 mV (Figure 7c). The high rate working performance of the cell could be endowed by the fast ion transport and interface behavior that moderate electrode polarization in particular of LTO-8.

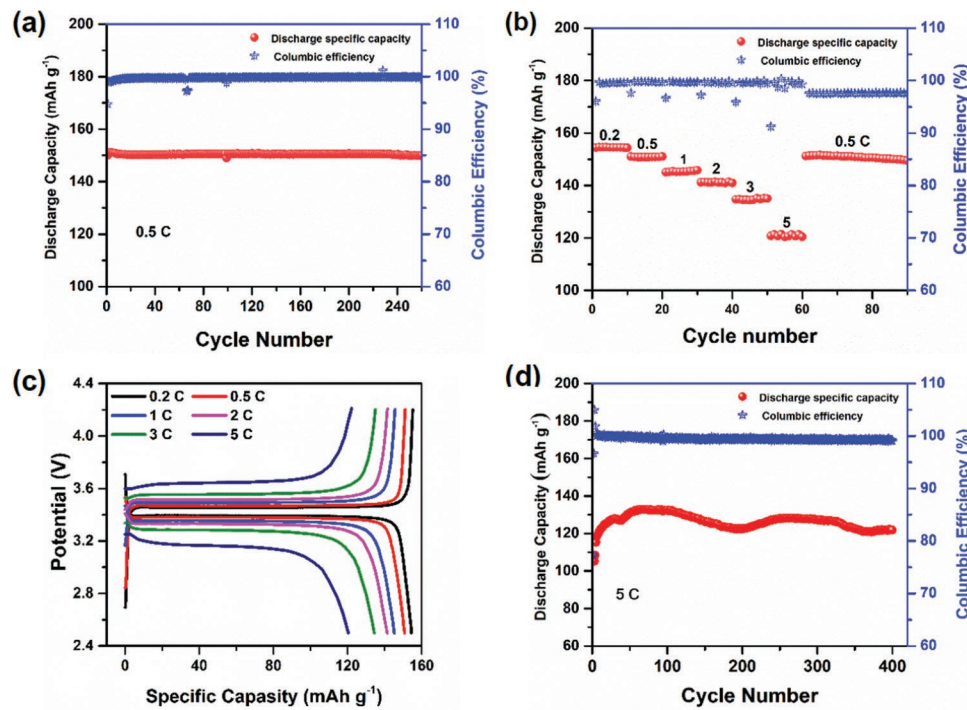


**Figure 7.** Galvanostatic cycling performance of Li|LTO-8|LFP cells at 35 °C, discharge capacity and columbic efficiency at a) 0.5C; b) capacity and c) potential profiles at different rate; d) cycling performance at 5C.

The Li|LTO-8|LFP cell were then cycled under 5C (Figure 7d). The capacity curve with wavy fluctuation delivers a considerable average specific capacity of 119 mAh g<sup>-1</sup> in 400 cycles. High current density could impose a larger overpotential and increase inhomogeneity of Li stripping/plating behavior at Li|LTO-8 interface. A redistribution of the mixed conductive interlayer is induced by greater electric field changes during charging/discharging and its hysteresis might account for capacity floating. A high columbic efficiency is sustained regardless capacity fluctuation, showing the electrochemical behavior still exhibits high reversibility.

Overall, LTO-8 containing highly concentrated Li<sub>4</sub>Ti<sub>5</sub>O<sub>12</sub> exhibited adequate high ionic conductivity. Its electrochemical activity builds an asymmetric structure that achieved good electrochemical stability against either anode or cathode. With the rational Li<sub>4</sub>Ti<sub>5</sub>O<sub>12</sub> proportion, LTO-8 presented a considerable excellent working performance in Li||LFP solid state cells such as cycling and rate behaviors.

### 3. Conclusions

In summary, we investigated the electrochemical behavior of Li<sub>4</sub>Ti<sub>5</sub>O<sub>12</sub> based SSEs incorporating with PVDF, and ensuring the optimal proportion of 80 wt% with stable performance. It is found that the ionic conductivity ( $2.87 \times 10^{-4}$  S cm<sup>-1</sup> at 35 °C) and ionic transfer number (0.87) are improved as Li<sub>4</sub>Ti<sub>5</sub>O<sub>12</sub> content increases to 80 wt%. The spontaneously formed interlayer at anode side achieves an asymmetry structure that adapts to electrode behavior, resulting to an outstanding interface stability. Li||LFP cells employing the

LTO-8 with 80 wt% of Li<sub>4</sub>Ti<sub>5</sub>O<sub>12</sub> show superior performance of 250 cycles with a stable discharge capacity of 150 mAh g<sup>-1</sup> under 0.5C, and a considerable average specific capacity of 119 mAh g<sup>-1</sup> under 5C in 400 cycles. Though dynamic evolution and theoretical mechanism, which could be verified by in-situ characterization and computational simulation, were less discussed in this work, the study puts forward another fresh point of view in the application promise of SSEs consisting of a considerable low cost, commercialized electrode material, Li<sub>4</sub>Ti<sub>5</sub>O<sub>12</sub>, and the true commercialization of SSBs will come soon.

### 4. Experimental Section

**Electrolyte Synthesis:** Spinel-type Li<sub>4</sub>Ti<sub>5</sub>O<sub>12</sub> (no carbon coating, white) with an average diameter of 500 nm was mixed with PVDF (130 000 wt) physically in different proportion, followed by ball milling at 500 rpm after the addition of isopropanol. Dimethylformamide (DMF) solvent was added into the as-dried mixture, and became homogeneous slurry after 6 h of vigorous stirring. The slurry was plate-coated on a PET released film, and dried in vacuum oven at 80 °C. The membrane removed from the substrate was cut into pieces for further characterization.

**LFP cathode preparation:** LiFePO<sub>4</sub>, PVDF and acetylene black mixed with a weight ratio of 8:1:1 were added into N-methyl-2-pyrrolidene (NMP). The slurry was magnetically stirred for 6 h and blade coated on aluminum foil. After placed in vacuum oven at 80 °C overnight, the cathode was cut into 10 mm diameter pieces, weighted, then stored in Argon-filled glove box.

**Characterization:** X-ray diffraction (XRD) was carried with Rigaku SmartLab3KW emitting Cu K $\alpha$  radiation over a 2 $\theta$  range of 10–90°. The structures of inner and surface of SSEs, as well as the lithium deposition morphology were photoed by the Philips scanning electron microscopy (SEM) XL70 with a voltage of 15 kV.

Raman spectra were recorded on a HORIBA Xplora Plus Raman microscope, employing an excitation wavelength of 532 nm. The acquisition time was 100 s for each Raman spectrum,

The coin cells were assembled in Argon-filled glove box. In case of pure PVDF, a drop of conventional nonaqueous carbonate electrolyte (LB315, 10  $\mu\text{L}$ ) was added during cell assembly to gelatinize polymer and wet the interface for further electrochemical test.

Solartron Analytical 1287A electrochemical workstation was used to test ionic conductivity of SSEs by AC electrochemical impedance spectroscopy (EIS) with an AC amplitude of 10 mV within the frequency from 1 MHz to 0.1 Hz. The test was conducted in temperature from 35 to 105 °C to estimate activation energy. The ionic conductivity and activation energy were calculated using the following equation:

$$\sigma = \frac{L}{RS} = A \exp \frac{-E_a}{TK_b} \quad (1)$$

where  $S$  is contact area of the SSE and electrode;  $L$  is thickness of the SSE;  $R$  is impedance between the SSE and block electrode;  $E_a$  is ion transport activation energy;  $A$  is pre-exponential factor;  $T$  is absolute temperature; and  $K_b$  is Boltzmann constant.

Electrochemical window of SSEs was tested by liner sweep scanning (LSV) from 0 to 6 V on Li|SSE|stainless steel (SS) cell. The  $\text{Li}^+$  transfer number ( $t_{\text{Li}^+}$ ) was obtained through potentiostatic experiment, in which 10 mV of step potential was applied on symmetry Li|SSE|Li cells for 1000 s to obtain initial and steady currents for calculation. Lithium stripping/plating behavior was characterized through galvanostatic experiment under 0.3 mA cm<sup>-2</sup> and critical current test under a lifting current density from 0.2 to 4 mA cm<sup>-2</sup> on Li|SSE|Li cells. Li|SSE|Cu cells were charged to 0 V at 0.1 mA cm<sup>-2</sup>, followed by 0.3 mA cm<sup>-2</sup> until the capacity reach 1 mAh cm<sup>-2</sup>.

Li|SSE|LFP cells were assembled to evaluate electrochemical performance by a LAND CT2001A battery test system at 35 °C. The long-term working stability was tested at 0.5C and 5C. The rate capability was tested from 0.2 C to 5 C within a potential range of 2.5 to 4.2 V. To get EIS plot changes in a cycle, the cell was tested for each 30 min or at 100% of SOC, and was left standing for 20 min before the measurement.

## Supporting Information

Supporting Information is available from the Wiley Online Library or from the author.

## Acknowledgements

The authors gratefully acknowledge the financial support from the National Key R & D Program of China (2021YFB2400200), the National Natural Science Foundation Committee of China (Key Project No. 52131306, Distinguished Youth Scientists Project No. 51425301), State Key Lab Research Foundation (ZK201805 and ZK201717), and Postgraduate Research & Practice Innovation Program of Jiangsu Province (KYCX20\_1072).

## Conflict of Interest

The authors declare no conflict of interest.

## Data Availability Statement

The data that support the findings of this study are available from the corresponding author upon reasonable request.

## Keywords

high ionic conductivity,  $\text{Li}_4\text{Ti}_5\text{O}_{12}$ , solid state battery, solid state electrolytes

Received: June 13, 2022

Revised: July 22, 2022

Published online: August 25, 2022

- [1] X. Zhang, Q. Xiang, S. Tang, A. Wang, X. Liu, J. Luo, *Nano Lett.* **2020**, 20, 2871.
- [2] P. G. Balakrishnan, R. Ramesh, T. Prem Kumar, *J. Power Sources* **2006**, 155, 401.
- [3] J. Tippens, J. C. Miers, A. Afshar, J. A. Lewis, F. J. Q. Cortes, H. Qiao, T. S. Marchese, C. V. Di Leo, C. Saldana, M. T. McDowell, *ACS Energy Lett.* **2019**, 4, 1475.
- [4] C. Sun, J. Liu, Y. Gong, D. P. Wilkinson, J. Zhang, *Nano Energy* **2017**, 33, 363.
- [5] H. Chang, Y.-R. Wu, X. Han, T.-F. Yi, *Energy Mater.* **2021**, 1, 100003.
- [6] D. Cai, X. Qi, J. Xiang, X. Wu, Z. Li, X. Luo, X. Wang, X. Xia, C. Gu, J. Tu, *Chem. Eng. J.* **2022**, 435, 135030.
- [7] Y. Zhu, X. He, Y. Mo, *J. Mater. Chem. A* **2016**, 4, 3253.
- [8] J. A. Lewis, F. J. Q. Cortes, M. G. Boebinger, J. Tippens, T. S. Marchese, N. Kondekar, X. Liu, M. Chi, M. T. McDowell, *ACS Energy Lett.* **2019**, 4, 591.
- [9] B. Gao, R. Jalem, Y. Tateyama, *ACS Appl. Mater. Interfaces* **2020**, 12, 16350.
- [10] J. Lu, Y. Li, Y. Ding, *Ceram. Int.* **2020**, 46, 7741.
- [11] J. Zhu, J. Zhao, Y. Xiang, M. Lin, H. Wang, B. Zheng, H. He, Q. Wu, J. Y. Huang, Y. Yang, *Chem. Mater.* **2020**, 32, 4998.
- [12] J. D. Howard, G. Evmenenko, J. J. Kim, R. E. Warburton, S. Patel, T. T. Fister, D. B. Buchholz, J. Greeley, L. A. Curtiss, P. Fenter, *ACS Appl. Mater. Interfaces* **2022**, 14, 7428.
- [13] J.-F. Wu, B.-W. Pu, D. Wang, S.-Q. Shi, N. Zhao, X. Guo, X. Guo, *ACS Appl. Mater. Interfaces* **2019**, 11, 898.
- [14] J. Zhang, C. Zheng, L. Li, Y. Xia, H. Huang, Y. Gan, C. Liang, X. He, X. Tao, W. Zhang, *Adv. Energy Mater.* **2020**, 10, 1903311.
- [15] M. Müller, J. Schmieg, S. Dierickx, J. Joos, A. Weber, D. Gerthsen, E. Ivers-Tiffée, *ACS Appl. Mater. Interfaces* **2022**, 14, 14739.
- [16] M. Cai, J. Jin, T. Xiu, Z. Song, M. E. Badding, Z. Wen, *Energy Storage Mater.* **2022**, 47, 61.
- [17] M. Du, Y. Sun, B. Liu, B. Chen, K. Liao, R. Ran, R. Cai, W. Zhou, Z. Shao, *Adv. Funct. Mater.* **2021**, 31, 2101556.
- [18] S. Kim, H. Kim, K. Thomas-Alyea, G. Yoon, B. Kim, M. Badding, Z. Song, J. Chang, J. Kim, D. Im, K. Kang, *Adv. Energy Mater.* **2020**, 10, 1903993.
- [19] Y. Liu, C. Li, B. Li, H. Song, Z. Cheng, M. Chen, P. He, H. Zhou, *Adv. Energy Mater.* **2018**, 8, 1702374.
- [20] R. J. Y. Park, C. M. Eschler, C. D. Fincher, A. F. Badel, P. Guan, M. Pharr, B. W. Sheldon, W. C. Carter, V. Viswanathan, Y.-M. Chiang, *Nat. Energy* **2021**, 6, 314.
- [21] J. Meng, Y. Zhang, X. Zhou, M. Lei, C. Li, *Nat. Commun.* **2020**, 11, 3716.
- [22] Y. Shao, H. Wang, Z. Gong, D. Wang, B. Zheng, J. Zhu, Y. Lu, Y.-S. Hu, X. Guo, H. Li, *ACS Energy Lett.* **2018**, 3, 1212.
- [23] Y. Zhong, Y. Xie, S. Hwang, Q. Wang, J. J. Cha, D. Su, H. Wang, *Angew. Chem., Int. Ed.* **2020**, 59, 14003.
- [24] H. Huo, Y. Chen, R. Li, N. Zhao, J. Luo, J. G. Pereira da Silva, R. Mücke, P. Kaghazchi, X. Guo, X. Sun, *Energy Environ. Sci.* **2020**, 13, 127.
- [25] J. Xu, Y. Meng, Q. Ding, R. Wang, T. Gan, J. Zhang, Z. Lin, J. Xu, *J. Mater. Chem. A* **2022**, 10, 4402.

- [26] S. Li, J. Lu, Z. Geng, Y. Chen, X. Yu, M. He, H. Li, *ACS Appl. Mater. Interfaces* **2022**, <https://doi.org/10.1021/acsami.1c21804>.
- [27] P. Jiang, J. Cao, B. Wei, G. Qian, S. Wang, Y. Shi, G. Du, X. Lu, C. Ouyang, F. Cao, X. Lu, *Energy Storage Mater.* **2022**, *48*, 145.
- [28] H. Kim, C. Im, S. Ryu, Y. J. Gong, J. Cho, S. Pyo, H. Yun, J. Lee, J. Yoo, Y. S. Kim, *Adv. Funct. Mater.* **2021**, *32*, 2107555.
- [29] L. Ye, X. Li, *Nature* **2021**, *593*, 218.
- [30] J. Wu, L. Yuan, W. Zhang, Z. Li, X. Xie, Y. Huang, *Energy Environ. Sci.* **2020**, *14*, 12.
- [31] Y. Lu, C.-Z. Zhao, H. Yuan, J.-K. Hu, J.-Q. Huang, Q. Zhang, *Matter* **2022**, *5*, 876.
- [32] W. Zhang, J. Nie, F. Li, Z. L. Wang, C. Sun, *Nano Energy* **2018**, *45*, 413.
- [33] S. H. Siyal, S. S. A. Shah, T. Najam, M. S. Javed, M. Imran, J.-L. Lan, *ACS Appl. Energy Mater.* **2021**, *4*, 8604.
- [34] L. Shen, S. Deng, R. Jiang, G. Liu, J. Yang, X. Yao, *Energy Storage Mater.* **2022**, *46*, 175.
- [35] Q. Yi, W. Zhang, T. Wang, J. Han, C. Sun, *Energy Environ. Mater.* **2022**, <https://doi.org/10.1002/eem2.12289>.
- [36] X. Ban, W. Zhang, N. Chen, C. Sun, *J. Phys. Chem. C* **2018**, *122*, 9852.
- [37] J. Bi, D. Mu, B. Wu, J. Fu, H. Yang, G. Mu, L. Zhang, F. Wu, *J. Mater. Chem. A* **2020**, *8*, 706.
- [38] D. Li, L. Chen, T. Wang, L.-Z. Fan, *ACS Appl. Mater. Interfaces* **2018**, *10*, 7069.
- [39] W. Fitzhugh, X. Chen, Y. Wang, L. Ye, X. Li, *Energy Environ. Sci.* **2021**, *14*, 4574.
- [40] E. Yi, H. Shen, S. Heywood, J. Alvarado, D. Y. Parkinson, G. Chen, S. W. Sofie, M. M. Doeff, *ACS Appl. Energy Mater.* **2020**, *3*, 170.
- [41] Y. Li, D. Cao, W. Arnold, Y. Ren, C. Liu, J. B. Jasinski, T. Druffel, Y. Cao, H. Zhu, H. Wang, *Energy Storage Mater.* **2020**, *31*, 344.
- [42] C. Han, Y.-B. He, S. Wang, C. Wang, H. Du, X. Qin, Z. Lin, B. Li, F. Kang, *ACS Appl. Mater. Interfaces* **2016**, *8*, 18788.
- [43] H.-K. Tian, R. Jalem, B. Gao, Y. Yamamoto, S. Muto, M. Sakakura, Y. Iriyama, Y. Tateyama, *ACS Appl. Mater. Interfaces* **2020**, *12*, 54752.
- [44] Z. Lu, J. Yu, J. Wu, M. B. Effat, S. C. T. Kwok, Y. Lyu, M. M. F. Yuen, F. Ciucci, *Energy Storage Mater.* **2019**, *18*, 311.
- [45] D. Zhang, X. Xu, X. Huang, Z. Shi, Z. Wang, Z. Liu, R. Hu, J. Liu, M. Zhu, *J. Mater. Chem. A* **2020**, *8*, 18043.
- [46] Z. Xu, T. Yang, X. Chu, H. Su, Z. Wang, N. Chen, B. Gu, H. Zhang, W. Deng, H. Zhang, W. Yang, *ACS Appl. Mater. Interfaces* **2020**, *12*, 10341.
- [47] S.-S. Chi, Y. Liu, N. Zhao, X. Guo, C.-W. Nan, L.-Z. Fan, *Energy Storage Mater.* **2019**, *17*, 309.
- [48] Z. Wan, D. Lei, W. Yang, C. Liu, K. Shi, X. Hao, L. Shen, W. Lv, B. Li, Q. H. Yang, *Adv. Funct. Mater.* **2019**, *29*, 1805301.
- [49] H. Huo, Y. Chen, J. Luo, X. Yang, X. Guo, X. Sun, *Adv. Energy Mater.* **2019**, *9*, 1804004.
- [50] C. Wang, Q. Sun, Y. Liu, Y. Zhao, X. Li, X. Lin, M. N. Banis, M. Li, W. Li, K. R. Adair, D. Wang, J. Liang, R. Li, L. Zhang, R. Yang, S. Lu, X. Sun, *Nano Energy* **2018**, *48*, 35.
- [51] Z. Hong, V. Viswanathan, *ACS Energy Lett.* **2018**, *3*, 1737.
- [52] K. Mukai, Y. Kato, H. Nakano, *J. Phys. Chem. C* **2014**, *118*, 2992.
- [53] L. Aldon, P. Kubiak, M. Womes, J. C. Jumas, J. Olivier-Fourcade, J. L. Tirado, J. I. Corredor, C. Pérez Vicente, *Chem. Mater.* **2004**, *16*, 5721.
- [54] Y. Chen, Z. Wang, X. Li, X. Yao, C. Wang, Y. Li, W. Xue, D. Yu, S. Y. Kim, F. Yang, *Nature* **2020**, *578*, 251.
- [55] X. Xiong, W. Yan, Y. Zhu, L. Liu, L. Fu, Y. Chen, N. Yu, Y. Wu, B. Wang, R. Xiao, *Adv. Energy Mater.* **2022**, *12*, 2103112.
- [56] Z. Li, S. Zhang, K. Qian, P. Nie, S. Chen, X. Zhang, B. Li, T. Li, G. Wei, F. Kang, *iScience* **2020**, *23*, 101636.
- [57] J. Gao, J. Zhu, X. Li, J. Li, X. Guo, H. Li, W. Zhou, *Adv. Funct. Mater.* **2021**, *31*, 2001918.
- [58] T. Zeng, X. Hu, P. Ji, B. Shang, Q. Peng, Y. Zhang, R. Song, *J. Power Sources* **2017**, *359*, 250.
- [59] N. Ohta, K. Takada, L. Zhang, R. Ma, M. Osada, *Adv. Mater.* **2006**, 2226.
- [60] J. Liu, X. Gao, G. O. Hartley, G. J. Rees, C. Gong, F. H. Richter, J. Janek, Y. Xia, A. W. Robertson, L. R. Johnson, P. G. Bruce, *Joule* **2020**, *4*, 101.
- [61] J. Illig, M. Ender, T. Chrobak, J. P. Schmidt, D. Klotz, E. Ivers-Tiffée, *J. Electrochem. Soc.* **2012**, *159*, A952.
- [62] J. P. Schmidt, T. Chrobak, M. Ender, J. Illig, D. Klotz, E. Ivers-Tiffée, *J. Power Sources* **2011**, *196*, 5342.
- [63] P. Shafiei Sabet, D. U. Sauer, *J. Power Sources* **2019**, *425*, 121.